Dynamical Stability of Polar Circumbinary Orbits and Planet Formation in the Planetary Disk of 99 Herculis

Ying Wang[1] , Wei Sun[1] , Ji-lin Zhou[2] , Ming Yang[3] , and Fu-yao Liu[1]

[1] School of Mathematics, Physics and Statistics, Shanghai University of Engineering Science, Shanghai 201620, People's Republic of China; wangying424524@163.com, sunweiay@163.com, liufuyao2017@163.com

[2] School of Astronomy and Space Science and Key Laboratory of Modern Astronomy and Astrophysics in Ministry of Education, Nanjing University, Nanjing 210093, People's Republic of China; zhoujil@nju.edu.cn

[3] College of Surveying and Geo-Informatics, Tongji University, Shanghai 200092, People's Republic of China; ming.yang@nju.edu.cn

Abstract

A possible polar-ring debris disk, the dynamics of which can be described by the outer hierarchical restricted three-body problem, has been detected in 99 Herculis. An empirical formula for the minimum radius beyond which test particles in polar orbits can keep stable within 10^7 binary periods is provided through numerical fitting, applying to the binary eccentricity $e_1 \in [0, 0.8]$ and the mass ratio of the binary $\lambda \in [0.1, 1]$, where $\lambda = m_0/m_1$ (m_0 and m_1 represent the masses of the two binary stars). The polar planetary disk has the lowest statistical accretion efficiency and a moderate impact frequency of collisions among planetesimals (with radii of 1–10 km) compared to those in a circumbinary coplanar disk and a standard disk around the single host star. The collision timescale in the circumbinary disk (both polar and coplanar configurations) is longer than 10^7 yr, exceeding the dissipation timescale of the gas disk. Stochastic simulations show that successive collisions cannot make planetesimals grow, which may explain the formation of the debris disk observed in 99 Herculis.

1. Introduction

Up until 2023 January, approximately 737 planets have been discovered in binary systems.[4] These planets in binary systems can be classified into three types according to their orbital configuration: *S*-type (satellite-type), *P*-type (planet-type), and *L*-type (libration-type; Dvorak 1986). Planets in *S*-type orbits, which are also called circumprimary planets, encircle one of the stellar binary components with the second star considered to be a perturber. Planets in *P*-type orbits, also known as circumbinary planets, encircle both members of the binary. *L*-type planets librate around the Lagrangian equilibrium points L_4 or L_5, which can stably exist if the total binary mass satisfies $\mu < 0.04$, where $\mu = m_0/(m_0 + m_1)$. The currently observed exoplanets in circumbinary systems include approximately 75 *P*-type planets, and the others are *S*-type planets.[5]

Planetary formation in binary systems is different from that in single-star systems because of the disturbance from the movements of the binary stars. The planetary disk will be truncated during several binary periods (Artymowicz & Lubow 1994), and forced into eccentric and processional motions (Larwood et al. 1996; Paardekooper et al. 2008; Fragner & Nelson 2010). The planets can also be forced into noncircular orbits by disk eccentricity. The inward migration of planets will be stalled upon entrance to the tidally truncated inner cavity in hydrodynamical simulations of the formation of *P*-type planets in the Kepler 16, 34, and 35 systems (Pelupessy & Zwart 2013;

Pierens & Nelson 2013). 2D locally isothermal hydrodynamical simulations of circumbinary disks with embedded planets were performed by Penzlin et al. (2021). The results strongly support the assumption that planets migrate to their present locations due to planet–disk interaction. During the migration, circumbinary planets could be captured into mean motion resonances, which may be associated with their final locations (Gianuzzi et al. 2023).

Some *P*-type planets were detected close to the edges of stable regions, where disturbances are remarkably powerful to form planets, even considering the most favorable case of 100% efficient dust accretion (Moriwaki & Nakagawa 2004; Meschiari 2012; Paardekooper et al. 2012; Martin & Triaud 2014). Moreover, the self-gravity of the circumbinary disk can excite eccentricities and prevent a full alignment of the planetesimal pericenters, thus resulting in sufficiently large impact velocities among planetesimals that damage the impacting planetesimals in the current locations of circumbinary planets (Marzari et al. 2013). The accretion of planetesimals is possible for $a_2/a_1 > 20$ in Kepler 16 (Marzari et al. 2012; Meschiari 2012; Paardekooper et al. 2012), where a_1 and a_2 are the semimajor axes of the binary and planetesimals, respectively. The gravity of an axisymmetric disk strongly suppresses the eccentricities of planetesimals beyond $a_2/a_1 \approx 10$–20, facilitating the easy growth of 1–10^2 km objects (Rafikov 2013a). The critical radial distance beyond which planetesimal accretion is possible increases with rising binary eccentricity and decreasing mass ratio, based on an examination of the relative velocities among accreting planetesimals (Scholl et al. 2007).

In addition to the difficulties of circumbinary planet formation at observed locations, the stable region around the binary where planets can survive for long times must be identified as a fundamental question of celestial mechanics.

Holman & Wiegert ([1999](#)) simulated the empirical criteria for the largest and the smallest stable orbits of test particles in the orbital planes of S-type and P-type binaries within $10^4 T_1$ (T_1 is the binary period) in the range $0.0 \leqslant e_1 \leqslant 0.7$–$0.8$ and $0.1 \leqslant \mu \leqslant 0.5$. Many factors could influence the stability of planets during and after the postoligarchic evolution. Hong & van Putten ([2019](#)) extended the analysis of the chaotic region of coplanar P-type orbits by Dvorak ([1986](#)) to the unrestricted three-body problem and counterrotating orbits. Mean motion resonances between P-type planets can interact with the binary via resonant and secular effects, creating additional instabilities and driving chaos in multiplanet resonant systems (Sutherland & Kratter [2019](#)). Thun & Kley ([2018](#)) found that massive planets can significantly alter the disk structure and remain on nearly circular orbits based on the planet–disk mass ratio, while low-mass planets are strongly influenced by the disk, with eccentricities excited to high values. If additional planets formed in the circumbinary disk, planet–planet scattering, which takes place near the location of the currently discovered circumbinary planets, left a single planet with low eccentricity with 90% possibility (Gong [2016](#)).

Most of circumbinary planets are detected by transiting and eclipse time variations. Detected circumbinary planets are usually in the coplanar plane with binary orbits due to the restrictions of the two observational methods. Interestingly, several misaligned circumbinary planetary disks have been detected. The precessional circumbinary-ring model, which is mildly misaligned with the binary orbital plane by $10°$–$20°$, has successfully interpreted the observations of KH 15D from 1995 to 2012 (Chiang & Murray-Clay [2004](#); Winn et al. [2004](#); Capelo et al. [2012](#)).

Lacour et al. ([2016](#)) found that the binary orbital plane of HD 142527 inclines $70°$ relative to the outer circumbinary disk, which was considered as a transition disk. Through 3D hydrodynamical simulations of HD 142527, Price et al. ([2018](#)) confirmed that all of the main observational features such as the spirals, shadows, and horseshoe can be explained by interactions between the disk and the inner binary. However, there is no consensus on the inclination of the disk, which was considered to account for the optical asymmetry of the dust. Different methods find different solutions, which mainly range from $20°$ to $28°$ (Avenhaus et al. [2017](#); Hunziker et al. [2021](#)).

The circumbinary debris disk in the 99 Herculis system was resolved, which may move in the plane perpendicular to the binary pericenter direction (Kennedy et al. [2012](#)). The misalignment δi between the young circumbinary protoplanetary disk around the GG Tau A binary system in the quadruple system GG Tau, and the binary orbit is approximately $25°$–$50°$ (Cazzoletti et al. [2017](#); Aly et al. [2018](#)). Each stellar component of IRS43 has its own circumstellar disk, and both are surrounded by a highly inclined circumbinary disk ($>60°$; Brinch et al. [2016](#)). An unusual gas-rich circumbinary disk in the young HD 98800 system is probably in a polar configuration based on a simulation of the disk dynamics, and the physical properties of the disk are similar to those around young single stars (Verrier & Evans [2008](#); Kennedy et al. [2019](#)). The disk size (5–5.5 au) makes it one of the smallest disks known (Ribas et al. [2018](#)). Ziglin ([1975](#)) described the doubly averaged outer-restricted elliptic three-body problem, considering quadrupole approximation for the first time. HD 98800, which is a quadruple system, can be well

approximated as a hierarchical triple-star system. High-inclination particles were found in long-term stable orbits inclined by $55°$–$135°$ to the inner binary. During a study on disk formation, Verrier & Evans ([2009](#)) found that inclination variations and nodal precession caused by the inner binary for certain initial longitudes can suppress Kozai cycles that would otherwise occur due to the outer star in the hierarchical three-body problem. Farago & Laskar ([2010](#)) provided a complete analytical description of test particles in the secular and quadrupolar approximations of the outer hierarchical three-body problem using a vectorial formalism.

Given the stability of the inclined orbits, Pilat-Lohinger et al. ([2003](#)) recorded the escape time for inclined P-type orbits ($0° \leqslant i \leqslant 50°$) in equal-mass binary systems, with the binary eccentricity ranging from 0 to 0.5 within the integration time $5 \times 10^4 T_1$, and distinguished different types of motions using the fast Lyapunov indicator. Doolin & Blundell ([2011](#)) studied the stability of the inclined orbits of circumbinary test particles and found the critical radius of stable planets in polar orbits is smaller than that in coplanar orbits. Considering the mass of the planet as well as interactions between the planet and binary, Chen et al. ([2019](#)) extend the polar orbit to the generalized polar orbit by stationary inclinations, where the precession rates of the binary and planet are the same, and the relative inclination between the orbital plane of the planet and the binary are fixed. In contrast to retrograde circulating orbits being usually the most stable around binaries with small eccentricities, polar planets around highly eccentric binaries are the most stable (Chen et al. [2020](#)). N-body simulations were conducted to scan the Δe, $\Delta \Omega_2$, and chaos indicators to study the global stability for different λ of the binary and initial Ω of the polar orbits by Cuello & Giuppone ([2019](#)).

However, an empirical formula for the critical radius of stable polar orbits has not been obtained, and the possibility of planet formation in circumbinary polar disks remains unknown. This paper aims to address these two issues. First, the motions of test particles in polar orbits are briefly described considering an analysis of the elliptically restricted three-body problem in Section [2](#), which displays a libration mechanism in the longitude of the ascending node and the inclination relative to the plane of the binary. Then, an empirical formula of the stable boundary of circumbinary test particles in polar orbits with the longest integration time $10^7 T_1$ is presented in Section [3](#). The binary eccentricity is in the range of [0, 0.8], and the mass ratio range of the binary star is $\lambda = [0.1, 1]$. Lastly, statistical analyses and stochastic simulation of collisions among planetesimals in polar-ring disks are conducted to compare with the results of the coplanar circumbinary disk and standard disk around a single star in Section [4](#).

2. Circumbinary Polar Motion in the Outer-restricted Hierarchical Three-body Problem

The complete Hamiltonian of the hierarchical three-body system can be described in Jacobian coordinates. The hierarchical three-body secular approximation (Harrington [1968](#), [1969](#)) can be obtained by adopting Delaunay's canonical elements, considering the quadrupole moment, and averaging the Hamiltonian over short timescales by a von Ziepel transformation (Kozai [1962](#); Harrington [1968](#)). In the outer-restricted three-body problem, the outer body is assumed to be a massless test particle revolving around the binary pair; thus the outer body does not affect the inner orbit. Let the longitude
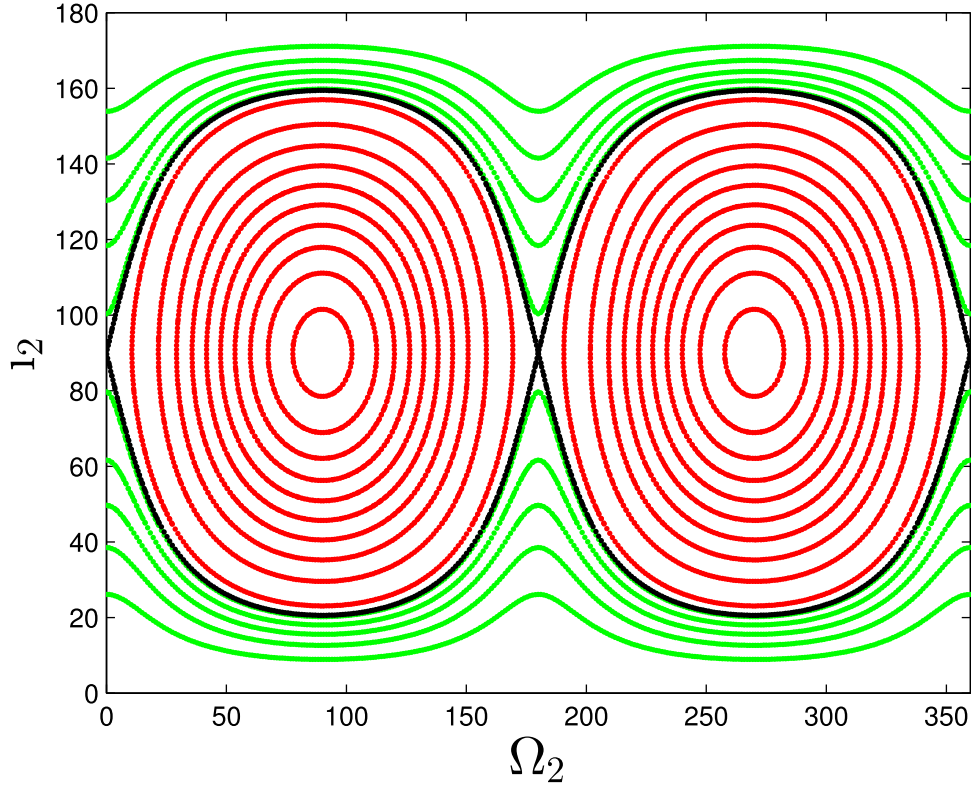
Figure 1. The phase space (Ω_2, i_2) of the simplified Hamiltonian in Equation (1) for 99 Herculis. The red region is the libration zone where the inclination and longitude of the outer orbit ascending node librate in a certain range. The green region is the circulation zone where the longitude of the outer orbit ascending node can circulate in [0°, 360°]. The black line is the separatrix between circulation and libration in Equation (2).

and pericenter of the inner orbit satisfy $g_1 + h_1 = \pi$ without losing generality. This condition, combined with the nodal difference between the two orbits in the invariable plane reference system meets $h_1 - h_2 = \pi$, leading to some orbital elements of the inner binary being eliminated from the general quadrupole Hamiltonian (Ford et al. 2000; Naoz et al. 2013). Omitting constant terms, a "simplified Hamiltonian" is obtained as follows,

$$H = (1 - e_1^2 + 5e_1^2 \sin^2 \Omega_2)\sin^2 i_2, \qquad (1)$$

where e_1 is the eccentricity of the inner binary orbit, Ω_2 is the longitude of outer orbit ascending node, and i_2 is the inclination of the outer orbit relative to the orbital plane of the binary.

The range of H is $[0, 1 + 4e_1^2]$. The separatrix between circulation and libration of Ω_2 is decided by the following,

$$H_c = 1 - e_1^2. \qquad (2)$$

The ascending node of the test particle librates near 90° or $-90°$ when $1 + 4e_1^2 > H > H_c$. Simultaneously, the inclination oscillates. The maximum and minimum of inclination appear when $|\Omega_2| = 90°$.

A possible polar-ring debris disk was detected in 99 Herculis by the Herschel Key Program Dust Emission via a Bias-free Reconnaissance in the Infrared/Submillimeter (DEBRIS). This program characterized extrasolar analogs to the asteroid and Kuiper belts of the solar system, which are collectively called "debris disks" (Pilbratt et al. 2010). 99 Herculis is a binary system, comprising an F7V primary (0.94 $M_\odot$) orbited by a K4V secondary (0.46 $M_\odot$) with an age of approximately 9.37 Gyr. The semimajor axis of the binary is approximately 16.5 au and its eccentricity is approximately 0.766. The

Herschel Key Program DEBRIS discovered a debris disk located at 120 au surrounding the binary. This disk is possibly a polar-ring debris disk, moving in a plane perpendicular to the binary pericenter direction and having a comparable lifetime with the star (Kennedy et al. 2012).

The phase space (Ω_2, i_2) of the simplified Hamiltonian by Equation (1) is plotted for $e_1 = 0.799$ (the binary eccentricity for 99 Herculis; Kennedy et al. 2012) in Figure 1. When $|\Omega_2| = 90°$, if the inclination of the orbital plane is larger than approximately 21°, then the test particle will be deep in the libration zone with the inclination librating within [21°, 159°].

A theoretical analysis of the outer-restricted hierarchical problem is provided in this section to describe the circumbinary polar orbit in the quadrupole approximation briefly. However, the long-term stability of polar orbits remains unknown. Only the quadrupole term is considered for the theoretical analysis based on the expansion of the complete Hamiltonian using the ratio of the semimajor axis of the inner orbit to that of the outer one. The orbits may show different movements in the octupole Hamiltonian. For example, the eccentricity of near-polar orbits may be significantly excited (Li et al. 2014). Therefore, numeric calculations are necessary to investigate the stability of polar orbits with different orbital elements. Next, the stable region of test particles in polar orbits of the outer-restricted hierarchical three-body problem will be presented.

3. The Innermost Stable Orbits of Test Particles in Polar Orbits

Pilat-Lohinger et al. (2003) recorded the escape time of inclined P-type orbits (0° ⩽ i ⩽ 50°) in binary systems with equal masses and eccentricities of 0 ⩽ e_1 ⩽ 0.5. If the binary

eccentricity is larger than 0.35, then the critical inclination for libration will be smaller than $50°$ for equal-mass binary systems. Therefore, the simulations with $0.4 \leqslant e_1 \leqslant 0.5$ in the article (Pilat-Lohinger et al. 2003) may include circulation and libration orbits. Their results revealed an absence of stable orbits with high inclinations over those with low inclinations. However, the numerical simulations of an equal-mass binary with $0.4 \leqslant e_1 \leqslant 0.5$ in the paper of Doolin & Blundell (2011) show that the high inclination of prograde orbits can be beneficial to stability compared with near-coplanar prograde orbits. The results of Pilat-Lohinger et al. (2003) and Doolin & Blundell (2011) seem in conflict, but they are not. The critical inclination for libration, $i_c = \arcsin\sqrt{\frac{H}{1 + 4e_1^2}}$, is determined at $h_2 = 90°$. Pilat-Lohinger et al. (2003) did not fix the longitude of ascending node of the planetary orbits specifically according to the separatrix between circulation and libration. They chose Ω_2 arbitrarily, finding that the critical inclination turning into the libration zone can be quite larger than i_c, as revealed in Figure 1. The critical inclination turning into libration for the arbitrary node can be obtained by the following,

$$i_\Omega = \arcsin\sqrt{\frac{H_c}{1 - e_1^2 + 5e_1^2 \sin^2 h_2}}. \tag{3}$$

Doolin & Blundell (2011) presented a density plot of the stability measure across entire parameter spaces with the longest integration time $5 \times 10^4 T_1$. First, peninsulas of instability in the libration region, which appear symmetrically on either side of $i = \pi/2$ for binary eccentricities of $e_1 \geqslant 0.3$, converge upon each other as $e_1 \rightarrow 0.6$. This result implies that high binary eccentricities of $e_1 \geqslant 0.6$ could be more favorable to the stability of orbits in the libration region compared with $0.3 \leqslant e_1 < 0.6$. The innermost semimajor axis of stable orbits in the libration region is smaller than that of stable prograde orbits in the circulation region. This finding means that the critical semimajor axis of stable planets in polar orbits is smaller than that of coplanar prograde orbits, thus raising the possibility of planet formation in polar planetary disks. An important point to note is that the innermost stable orbits in the libration region appear when the inclination of orbit is in the vicinity of $90°$, according to the stability maps in Doolin & Blundell (2011) and Cuello & Giuppone (2019). Here, we will find the innermost stable orbits for different binary parameters, namely the mass ratio of the binary star λ and the binary eccentricity e_1.

In order to obtain the innermost stable polar orbits, a large number of numerical simulations need to be carried out. Without loss of generality, the semimajor axis of the binary orbit is set as 1 au, and the binary eccentricity e_1 in the range [0, 0.8] with scanning interval $\Delta e_1 = 0.05$. Simultaneously, the mass ratio of the binary star $\lambda = [0.1, 1]$, where $m_0 = 1\ M_\odot$ and m_1 varies with an interval $0.05\ M_\odot$. The semimajor axes of test particles range from 2 to 6 au, with an interval of 0.01 au. For a specific semimajor axis, eight inclinations ware chosen from $\left[\arcsin\sqrt{\frac{H}{1 + 4e_1^2}}, 90°\right]$ with equal intervals. Eight mean anomalies are distributed evenly in the range $[0°, 360°]$ for each inclination. The initial longitude of ascending node h_2 is set as $90°$ in all cases. The orbits are circular initially, and the arguments of the pericenter are chosen arbitrarily. After $10^7 T_1$, the initial semimajor axes of the innermost orbits that remained stable are regarded as the critical stable boundary.

The following empirical formulas are computed using a multivariable linear regression analysis of the minimum stable semimajor axis a_c of test particles within $10^7 T_1$ with different binary mass ratio λ and eccentricity,

$$\begin{aligned} \frac{a_c}{a_1} = {} & 2.6338 + 4.9422e_1 + 0.7237\lambda \\ & - 3.6013e_1^2 - 1.1215\lambda^2 \\ & - 5.2632e_1\lambda + 5.3516e_1^2\lambda \\ & + 5.5769e_1\lambda^2 - 5.6002e_1^2\lambda^2, \end{aligned} \tag{4}$$

for $0.1 \leqslant \lambda \leqslant 1$, $0.0 \leqslant e_1 \leqslant 0.15$, and $0.65 \leqslant e_1 \leqslant 0.8$, with the coefficient of determination $R^2 \approx 1.0$, and,

$$\begin{aligned} \frac{a_c}{a_1} = {} & 4.4096 + 6.7118e_1 + 14.4955\lambda \\ & - 10.9044e_1^2 - 16.1753\lambda^2 \\ & - 60.3628e_1\lambda + 58.2231e_1^2\lambda \\ & + 54.8823e_1\lambda^2 - 46.2753e_1^2\lambda^2, \end{aligned} \tag{5}$$

for $0.1 \leqslant \lambda \leqslant 1$ and $0.25 \leqslant e_1 \leqslant 0.6$, with the coefficient of determination $R^2 \approx 0.8664$. Several fitted curves were plotted, and the corresponding raw data are presented in Figure 2.

Apparently, the tendencies of the minimum stable orbits with λ are different for the several eccentricity intervals shown in Figure 2. The values of the minimum stable semimajor axes of test particles moving in polar orbits around the binary with $e_1 = 0.2$ are directly plotted in Figure 2. The results with $e_1 = 0.2$ in addition to the fitting processes of Equations (4) and (5) did not yield good fitting effects, which can be seen in Table 1. The determination coefficient, F statistic, P value, and error variance after multiple regression fitting for different cuts are shown in the table below. It seems more appropriate to divide the data simulation into two parts, one part with eccentricity ranges of [0, 0.15] and [0.65, 0.8], and the other part with [0.25, 0.6].

For fixed binary eccentricity, a binary with comparable masses, $\lambda = 1$, is favorable to the stability of polar orbits. These orbits around the binary with mild eccentricities of $e_1 < 0.2$ can stably exist in locations closer to the binary compared with those around moderate and highly eccentric binaries. The stable boundary of polar orbits revolving the binary with high eccentricities of $e_1 > 0.6$ change slightly for different binary mass ratios. The numerical simulation of the stability of polar orbits revealed that finding planets in polar orbits at locations close to binary systems with comparable masses and mild eccentricities $e_1 < 0.2$ is more hopeful.

4. Accretion Efficiencies of Planetesimals in the Polar-ring Disk of 99 Herculis

It is possible the polar-ring disk in 99 Herculis resolved in Kennedy et al. (2012) is a debris disk that has undergone a stage of planet formation. Another possible polar-ring disk, in the young HD 98800 system, comprises a gas-rich "planet-forming" disk (Ribas et al. 2018; Kennedy et al. 2019). Zanazzi & Lai (2018) found that the timescale of the inclination evolution of a circumbinary disk under the influence of the disk warp profile and dissipative torque is shorter than the disk lifetime for typical disk parameters. Their finding implies that disks and planets may exist with high inclinations relative to the orbital plane of eccentric binaries. Based on hydrodynamic simulations, a series of articles
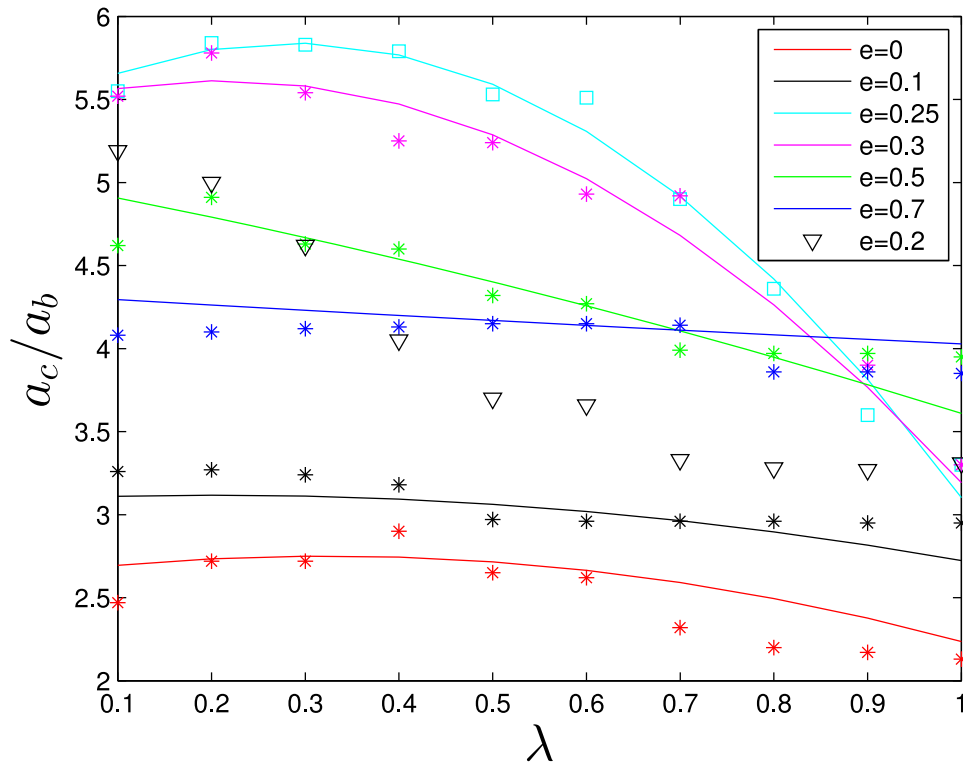
Figure 2. Several fitted curves of Equations (4) and (5), as well as the respective raw data of the minimum stable radii of test particles in polar orbits around binaries with different eccentricities and mass ratios within $10^7 T_1$.

Table 1
The Parameters from the Multiple Regression Fitting for Different Cuts of the Binary Eccentricity

e_1	R^2	F Statistic	P Value	Error Variance
[0, 0.8]	0.72	547.13	0	0.20
[0, 0.15] and [0.65, 0.8]	0.97	2917.30	0	0.015
[0.25, 0.6]	0.90	879.56	0	0.052
[0.2, 0.6]	0.76	350.71	3.37×10^{-269}	0.13
[0.3, 0.6]	0.87	560.09	4.34×10^{-296}	0.057

by Martin and Lubow (Martin & Lubow 2017, 2018, 2019) pointed out that damped oscillations of the tilt angle and longitude of ascending node of a misaligned low-mass protoplanetary disk around an eccentric binary lead to a stationary state where the disk lies perpendicular to the binary orbital plane. They revealed how the evolution of the disk depends upon the parameters of the disk (mass, viscosity, temperature, and size) as well as the parameters of the binary (binary mass ratio, orbital eccentricity, and inclination). The alignment timescale of the outer parts of sufficiently large disks may be longer than their dissipation timescale.

4.1. Initial Values of the Simulations

The formation of planets in a polar planetary disk (namely the polar case) is examined after determining the stable boundary of test particles in polar orbits. 99 Herculis was selected as the numerical model based on the assumption of an extended and young polar planetary disk. The accretion

efficiency of collisions among 30,000 planetesimals with randomly chosen physical radii from 1–10 km and density of 3 g cm^{-3} was investigated. Their orbital semimajor axes are evenly distributed in the range of 65–130 au. Therein, 65 au $\approx 3.94 a_1$ is the numerical stable boundary, which is consistent with $4.19 a_1$ obtained by Equation (4).

In two other cases, a coplanar disk of the same binary stars (namely the coplanar case) and a general disk around a single star (namely the standard case) were simulated for comparison. The "general disk" is based on the model of "minimum mass solar nebula," but with different scaling factors of the solid surface density and solid enhancement beyond the ice line (f_d and f_{ice}). The host in the standard case is a single star with a mass of 1.4 $M_\odot$ (the total mass of 99 Herculis).

Considering that the precession range of the orbital inclination in the polar disk is 10° for the initial inclination distributed in the range 85°–95°, in order to make the three planetary disks comparable, the orbital inclination ranges of the planetesimals in the coplanar disk and the standard disk were set to 0°–5° and the initial longitude of ascending nodes is chosen randomly.

In the numerical simulation, the orbits of planetesimals in planetary disks need to be as close as possible to the state of natural dynamic evolution, so as to reflect real collision results. If we start from circular orbits initially, the planetesimals in the polar disk need about 6×10^4 yr (about $10^3 T_1$, where T_1 is the binary period) to reach a natural state from a fixed initial longitude of ascending node at 90°, and need 9×10^5 yr (about $1.5 \times 10^4 T_1$) in the coplanar circumbinary disk from their initial circular orbits. Computing time costs are expensive for 30,000 planetesimals. So, we make efforts to let the planetesimals move initially naturally to the greatest extent on the basis of their dynamical properties.

In the polar protoplanetary disk, the initial inclination i is chosen in the range 85°–95° randomly. From the phase space and analytical theory of Li et al. (2014), the inclination oscillates in the following range,

$$\left[\arcsin\sqrt{\frac{H}{1+4e_1^2}}, \ \pi - \arcsin\sqrt{\frac{H}{1+4e_1^2}} \right]. \qquad (6)$$

So, we can obtain the range of initial longitude of ascending nodes of planetesimals $[\Omega_c, \pi - \Omega_c]$ for initial inclination i, which is chosen in the range 85°–95° randomly, where,

$$\Omega_c = \arcsin\sqrt{\left(\frac{(1+4e_1^2)\sin^2 i_c}{\sin^2 i} + e_1^2 - 1\right)\bigg/ 5e_1^2} \ \text{for} \ i_c = 85°. \qquad (7)$$

In an eccentric coplanar binary disk, considering the secular perturbations of the binary, the initial eccentricities of planetesimals are chosen in the range $[0, e_{\text{pump}}]$ arbitrarily (Moriwaki & Nakagawa 2004), where,

$$e_{\text{pump}} \simeq \frac{5}{2}\left(1 - \frac{m_1}{m_0 + m_1}\right)\frac{a_1}{a_2}e_1. \qquad (8)$$

The eccentricities of the planetesimals are chosen from 0–0.05 randomly in the general disk around the single star.

The inflated radii of planetesimals were adopted as $dr = 2r^{\frac{3}{2}}(GM)^{\frac{-1}{2}}d\nu$ (where $d\nu = 1\,\text{m s}^{-1}$ and M is the total mass of the binary) to trace close encounters between planetesimals easily (Xie & Zhou 2009), which can ensure an accuracy of the colliding velocity $\sim 1\,\text{m s}^{-1}$.

The inflated radius is artificially set to control the collision speed accuracy. In pure Kepler motion of the two-body problem, the velocity of the celestial body moving around the host satisfies $v = \left(\frac{GM}{r}\right)^{1/2}$. The differential of the formula can be obtained, $dr = 2r^{\frac{3}{2}}(GM)^{\frac{-1}{2}}d\nu$, which means that the velocity difference between two particles in Kepler motion at adjacent distance dr is $d\nu$. Therefore, the error between the relative velocity recorded here and the relative velocity of the collision can be guaranteed by limiting the distance, dr, between two adjacent planetesimals before the collision. This error is proportional to the distance; that is to say, the relative velocity recorded when the distance between planetesimals is smaller will be closer to the relative velocity at the time of collision. In our code, we judge whether the two planetesimals are within the critical distance, dr. On the one hand, the collision requires the two planetesimals to be in close contact. On the other hand, we can control the error range between the relative speed calculated within the critical distance and the realistic collision speed.

During our simulations, gas drag need not be considered because we found gas damping has little effect on the orbits of the planetesimals and collision results in our studies. On the one hand, for the outer part of the disk around 99 Her, which is located far away from the binary, the local gas density is too small to dampen the planetesimals. The gas damping force is proportional to the gas density and the relative velocity between the gas and the planetesimal. According to the general model of gas disk (Sano et al. 2000; Umebayashi et al. 2013), at midplane, the gas drag force at 66 au is 2.8×10^{-5} times than that at 1 au in the "minimum mass solar nebula." On the
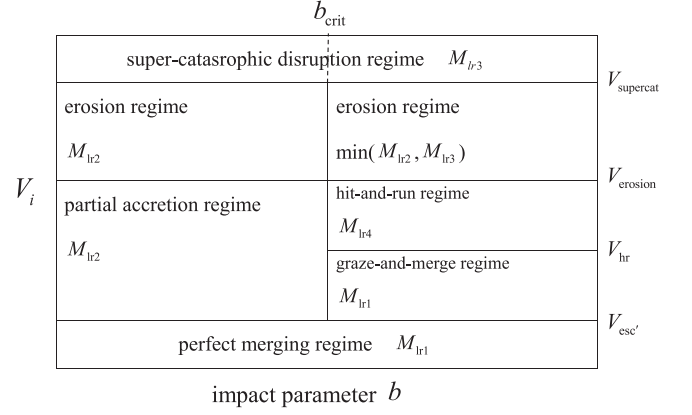

Figure 3. The outcomes of collisions mainly include seven regimes, which are determined by the impact velocity V_i as well as the impact factor b. The corresponding mass of the largest remnant can be calculated by the four equations $M_{\text{lr1}} = M_p + M_{\text{targ}}$, $M_{\text{lr2}} = (-0.5(Q_R/Q_{RD}'^* - 1) + 0.5)M_{\text{tot}}$, $M_{\text{lr3}} = \frac{0.1}{1.8^\eta}(Q_R/Q_{RD}'^*)^\eta M_{\text{tot}}$, and $M_{\text{lr4}} = M_{\text{targ}}$. Other variants appearing in these equations and in this figure can be found in Leinhardt & Stewart (2011) and Stewart & Leinhardt (2012).

other hand, for the inner part of the disk, the dynamics of the planetesimals are strongly excited by the binary, leading to the damping effect of the gas disk working inefficiently. Rafikov (2013a) found that gas drag does not resolve the fragmentation barrier issue in Kepler circumbinary systems because the fast relative precession of the planetesimal and binary orbits results in inefficient planetesimal apsidal alignment. Rafikov (2013b) also demonstrated that gas drag regulates the eccentricity behavior only for bodies with radii less than 1 km, which is below the adopted planetesimal size (1–10 km) in our article.

4.2. Outcomes of Collisions

During the realistic collisions among planetesimals, perturbations due to the gravitational force between the two planetesimals entering into the range of close encounters will gradually increase, which cannot be ignored. In our numerical simulations, gravitational interactions among planetesimals are neglected to save computation costs. We can use the physical parameters and the states of motion between the colliding planetesimals during entering into a close encounter to obtain the outcomes after collision approximately. The outcomes of collisions depend on the target mass M_{targ}, the projectile mass M_p, the target radius R_{targ}, the projectile radius R_p, the impact velocity V_i, as well as the impact factor b, which is defined as $b = \sin\theta$, where θ is the acute angle between the line of impact velocity and the barycenter line. The impact velocity vector $\vec{V_i}$ is the relative velocity between the target and the projectile. During our process to calculate the outcome of the collision between two bodies, we set the heavier one as M_{targ} and the lighter one M_p. Figure 3 summarized the regimes and the calculations of the mass of the largest remnant after each collision briefly. The detailed process and scaling laws used to calculate maps of collision outcomes can be found in Leinhardt & Stewart (2011) and Stewart & Leinhardt (2012).

We have tried three methods to deal with the results of collisions. In the first way, we assumed that the two planetesimals move in a straight line at a constant speed within the critical distance. A collision occurs when the distance between the planetesimals is less than the sum of the physical radii of the planetesimals. The statistical results show
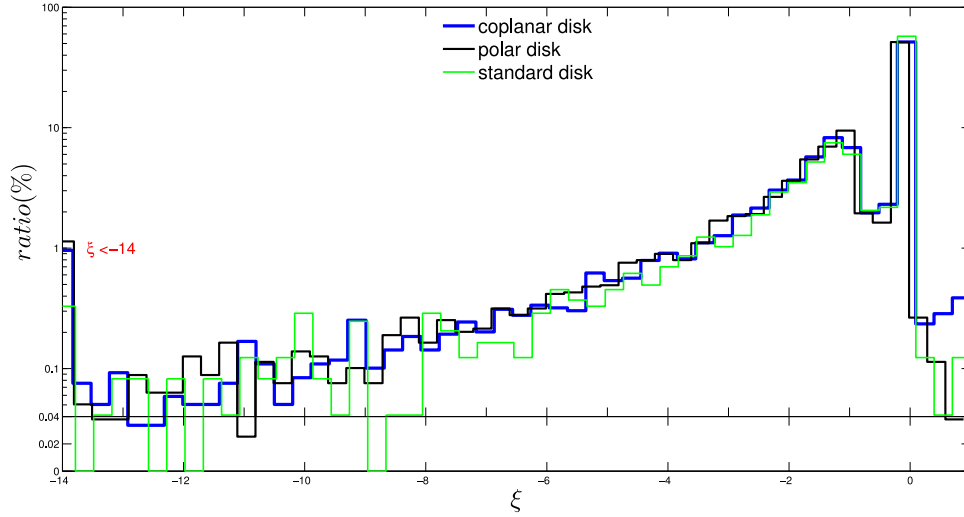
Figure 4. The collision outcomes among planetesimals in the polar protoplanetary disk of 99 Herculis system, the coplanar disk of the same binary stars (coplanar case), and the general disk around single stars with the mass of 99 Herculis system (standard case) for comparison. The coplanar case has the same initial conditions as the polar case except for the inclination, which is randomly chosen from 0°–5°. The standard case has the same initial conditions as the coplanar case except the host is a single star with mass 1.4 $M_\odot$, the total mass of 99 Herculis.

that almost no collisions have occurred, because this processing method ignores gravitational interactions between the planetesimals. In the second way, all of the collisions are regarded as head-on collisions and the diversity of actual collision results is ignored. The third way considers the collision parameters, and the calculation of the collision results is based on the coordinates and velocities of the planetesimals after they enter into the critical distance. This processing method will increase the proportion of hit-and-run collisions, which keeps the two planetesimals undamaged. However, we can eliminate the artificially enlarged effect of the hit-and-run regime by sufficient collisions. Considering that the growth of planetesimals requires multiple collisions, we made stochastic simulations to find out the final mass of the largest remnant for a specific planetesimal after successive collisions. As long as the cumulative number of collisions is sufficient, the artificially enlarged hit-and-run effect will be eliminated, and will not affect the final mass of the largest remnant. This is also the reason why we made statistical simulations in our article.

4.3. Efficiency of Accretion

The efficiency of accretion ξ is defined as follows,

$$\xi = \frac{M_{lr} - M_t}{M_p}, \tag{9}$$

where M_t is the mass of the target and M_p is the mass of projectile. M_{lr} is the largest mass of the remnant part after a collision between two planetesimals. The detailed calculations of M_{lr} can be obtained in Section 4.2. Clearly, $\xi = 1$ means that the two planetesimals have merged together, thus demonstrating perfect accretion. $0 < \xi < 1$ means collisions lead to partial accretion, and $\xi < 0$ implies target erosion.

The ratios of different efficiencies of accretion in the three disks are shown in Figure 4 and Table 2. There is one thing worth noticing: the peaks appearing in the vicinity of $\xi = 0$ include the overestimated part of hit-and-runs. Hit-and-runs can allow the planetesimals to be almost the same as before the collision, leading to $\xi \approx 0$. The perfect accretion ($\xi = 1$) in the polar-ring case is 0%, while those in the coplanar and standard

Table 2
A Brief Look at the Accretion Efficiency

	$\xi < 0$	$0 <= \xi < 0.5$	$0.5 =< \xi < 1$	$\xi = 1$	Collision Number
Polar case	50.81%	49.08%	0.1011%	0%	7915
Coplanar case	49.15%	50.29%	0.4372%	0.1261%	11,894
Standard case	44.17%	55.70%	0.08233%	0.04117%	2429

case are approximately 0.1261% and 0.04117%, respectively. Figure 4 shows that the accretion efficiencies among planetesimals that can cause accretion, including part and perfect accretion in the polar protoplanetary disk, are lower than either the coplanar binary disk or the single-star disk. Meanwhile, the erosion collision ($\xi < 0$) occurrence in polar-ring cases reveals slightly higher frequencies (50.81%) than those of the two other cases (49.15% and 44.17%). Because of the expensive computer costs, we only simulated one group for each case, so there are no error bars. If enough numerical simulations are conducted, the efficiencies of the accretion in the polar and coplanar circumbinary disks may be very close, presumably within the error bars. In general, collisions among the planetesimals in the polar protoplanetary disk are not favorable for accretion compared with the single-star disk.

According to the statistical data of the collision results, we can basically deduce that there is a high probability that planetesimals cannot grow through collisions. In view of the following two reasons, we continued to carry out stochastic simulations: on the one hand, the proportion of hit-and-run results was overestimated in the process of collision result processing, and it was necessary to eliminate its influence through enough collisions; on the other hand, stochastic simulations can give the maximum mass remaining quantitatively after a series of collisions.

Before stochastic simulations of successive collisions based on the ratios of efficiencies of accretion can be carried out, the collisional timescale require research, which determines the number of collisions that may occur within the age of 99 Herculis.
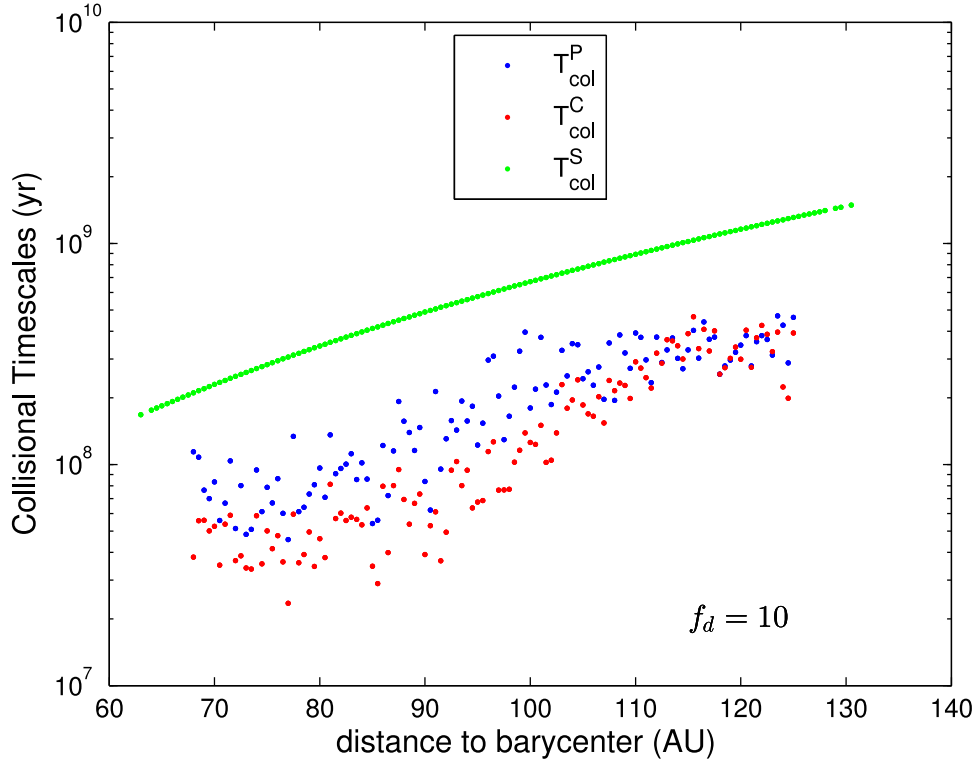
Figure 5. The collisional timescale of planetesimals in a polar circumbinary disk, $T_{\rm col}^{\rm P}$, and in a coplanar circumbinary disk, $T_{\rm col}^{\rm C}$, obtained by Equation (11) combined with Equation (10). The scaling factor of a solid surface density is set at a moderate value of $f_d = 10$.

4.4. Collisional Timescale

During the integration time of 10^5 yr, the numbers of collisions in the polar, coplanar, and standard cases are 7915, 11,894, and 2429, respectively, as shown in Table 2. Collisions among planetesimals occur most frequently in the coplanar case due to the strong dynamical disturbances from the binary. The number of collisions in the polar case is moderate for mild gravitational disturbances from the binary in the perpendicular plane, which affect the inclination more than the eccentricity. The average numbers of collisions in the polar and coplanar circumbinary disks are, respectively, three and five times as many as those in the standard disk surrounding the single star.

In single-star systems such as our solar system, the objects of the Kuiper Belt are distributed at 30–50 au from the Sun. The chance of collision among planetesimals will be remote considering the long period of such objects and the shortage of disturbances. Generally, the collisional timescale of planetesimals with typical radius R_p at semimajor axis a in the standard disk around a single star with mass M_A can be obtained by,

$$T_{\rm col}^{S} = \frac{2}{3} \times 10^4 f_{\rm d}^{-1} f_{\rm ice}^{-1} \left(\frac{a}{\rm au}\right)^3 \left(\frac{M_A}{M_\odot}\right)^{-1/2} \left(\frac{R_{\rm p}}{\rm km}\right) \ {\rm yr}, \quad (10)$$

where, for the "minimum mass solar nebula," $f_d = 1$ and $f_{\rm ice} = 4.2$ beyond the ice line, which lies at about 2.7 au for solar-type stars. According to Xie et al. (2009), the collisional timescales of planetesimals in a coplanar circumbinary disk $T_{\rm col}^{C}$

and in a polar circumbinary disk $T_{\rm col}^{P}$ can be estimated by,

$$T_{\rm col}^{C} = T_{\rm col}^{S} \times \left(\frac{n_{\rm imp}^{C}}{n_{\rm imp}^{S}}\right)^{-1},$$

$$T_{\rm col}^{P} = T_{\rm col}^{S} \times \left(\frac{n_{\rm imp}^{P}}{n_{\rm imp}^{S}}\right)^{-1}. \quad (11)$$

The impact rates $n_{\rm imp}^{S}$, $n_{\rm imp}^{C}$, and $n_{\rm imp}^{P}$ can be read out from our numerical simulations of the three disks containing the same total numbers and physical radius distribution of planetesimals.

Although the impact rates of circumbinary planetesimals are several times larger than in the standard disk, as shown in Figure 5, the collisional timescale $T_{\rm col}^{\rm P}$ of planetesimals in the polar circumbinary disk, and $T_{\rm col}^{\rm C}$ in the coplanar circumbinary disk with a moderate $f_d = 10$ are longer than 10^7 yr, which is beyond the observed dissipation timescale (<6 Myr) of gas disks (Haisch et al. 2001; Wyatt 2008). Ribas et al. (2015) confirmed that the dissipation timescale of a gas disk is directly related to the stellar mass. The gas disks around high-mass stars (>2 $M_\odot$) dissipate up to two times earlier than low-mass ones. That means gas giants hardly form in such distant locations through core accretion as the collisional timescales are too long to absorb enough gas. Next, stochastic simulations were conducted to find out whether solid cores of protoplanets can form.

4.5. Stochastic Simulations

However, Batygin & Brown (2016) show that a possible distant giant planet with more than 10 Earth masses in the solar

system can explain the clustering phenomenon of distant Kuiper Belt objects in the argument of perihelion and physical space. Kenyon & Bromley (2015) showed that super-Earth-mass planets can form at 125–250 au around solar-type stars from swarms of 1 cm–10 m planetesimals within 1–3 Gyr in the annuli with a mass of approximately 15 $M_\oplus$ considering collisional damping. However, this simulation did not include the gas drag, which is important for the vertical distribution and radial motion of dust and large bodies. The gas drag eventually becomes negligible once bodies of planetesimal size have formed.

After obtaining the probability distribution law which has been shown in Figure 4, we can obtain the probability density function. So that the efficiency of accretion of a random collision, ξ, can be obtained by the probability proportional to size sampling. The postcollision result can be calculated by the corresponding ξ. The mass of the largest remnant part M_{lr} after this collision, as one of the colliding planetesimals, participates in the next collision. After N random samplings, the final mass of the largest remnant after N consecutive random collisions can be obtained.

The reasons for conducting stochastic simulations are given below. On the one hand, we can eliminate the overestimated hit-and-run part through enough collisions. On the other hand, the distribution of the final growth mass of planetesimals can be obtained quantitatively. How many collisions are enough? First of all, we can obtain the number of collisions N_c by the collisional timescale within the age of 99 Herculis, which is about 9.37 Gyr. We conduct sampling for $100N_c$ in order to eliminate the overestimated hit-and-run part. The starting target planetesimal and the subsequent projectile ones have a physical radius of 10 km. There, we suppose there are sufficient planetesimals in protoplanetary disks. The detailed operations are as follows.

1. The discrete distribution function of the accretion efficiency, $F(\xi) = \sum_{\xi_n < \xi} p_n$, can be obtained using the data in Figure 4, for the distribution law below.

$$\begin{array}{c|ccc} \xi_1 & \xi_2 \cdots \xi_n \cdots \\ \hline p_1 & p_2 \cdots p_n \cdots \end{array}$$

2. Generate a random number ε from a uniform (0, 1) distribution.
3. For an ε, there must have an interval (ξ_{n-1}, ξ_n), making $F(\xi_{n-1}) < \varepsilon < F(\xi_n)$ with probability p_n.
4. For an ε, an accretion efficiency $\xi = (\xi_{n-1} + \xi_n)/2$ will be chosen. The mass of the largest remnant part after a collision will be calculated by Equation (9). The remnant continues to participate in the next collision.
5. If $\xi < -M_p/M_t$ leads to $M_{lr} < 0$, which is an unphysical result, we need to regenerate a random number ε.
6. Sampling with probability proportional to $100N_c$, then the final mass of planetesimal after enough collisions will be obtained.

We carry out 10,000 runs of probability proportional to the size sampling for the collisions occurring in each kind of protoplanetary disk. The distribution of the final largest mass of the remnant part M_{lr}/M_{ti} is listed in Table 3, where M_{ti} is the initial mass of the planetesimal before the collision. It is clear that the planetesimal can hardly grow bigger. In most cases, the final mass after $100N_c$ successive collisions is

Table 3
The Distribution of the Final Largest Mass of the Remnant Part M_{lr}/M_{ti} Among 10,000 Runs of Stochastic Simulations with $100N_c$ Successive Collisions

	M_{lr}/M_{ti}	Probability
Polar case	<0.97	19.93%
	[0.97, 1.05)	79.44%
	[1.05, 2]	0.63%
Coplanar case	<0.97	13.74%
	[0.97, 1.05)	84.47%
	[1.05, 2]	1.79%
Standard case	<0.97	11.61%
	[0.97, 1.05)	87.89%
	[1.05, 2]	0.5%

around the original mass at the beginning of the collisions. However, such a process may be a possible mechanism to produce dust continuously, making the debris disk observed in 99 Herculis. An older debris disk (>100 Myr) requires the replenishment of dust through mutual collisions among a population of greater-than-kilometer-sized planetesimals. Some of the youngest (about 10 Myr old) debris disks may be the remnants of protoplanetary disks (Wyatt & Dent 2002). 99 Herculis is a main-sequence star with an age of 6–10 Gyr. So, the debris disk observed asks for a dust-generation process whether it is a long-lived debris disk surviving for gigayear timescales or a transient ring generated from a recent collision. Our stochastic simulations show that the collisions of planetesimals in the polar protoplanetary disk of 99 Herculis will not make planetesimals grow, but produce dust steadily.

Since the molecular gas is collocated with the dust in the debris disk, a new semianalytical equivalent of the numerical model was proposed by Kral et al. (2016, 2017), which assumes CO is produced from volatile-rich solid bodies. P-type exoplanets in circumbinary coplanar orbits have been detected by Kepler (Martin & Triaud 2014). A majority of these planets are located at the boundary of stable zones over long timescales (Holman & Wiegert 1999). The stability limit is due to overlapping first- and second-order mean motion resonances with the binary, and is mainly influenced by the overlaps of three-body mean motion resonances in massive multiplanet systems (Wang et al. 2019). However, the formation of planets in the circumbinary coplanar disk is possible for $a_2 > 20a_1$ (Marzari et al. 2012; Meschiari 2012; Paardekooper et al. 2012), or $a \approx 10$–$20a_1$, considering the gravity of an axisymmetric disk which can strongly suppress the eccentricities of planetesimals beyond and facilitate the easy growth of planetesimals (Rafikov 2013a). Moreover, the critical radial distance beyond which planetesimal accretion is possible increases with the rising binary eccentricity (Scholl et al. 2007). Thus, planets can hardly form around 65–130 au (3.94–7.88a_1) in the circumbinary coplanar protoplanetary disk with $a_1 = 16.5$ au and $e_1 = 0.76$ of 99 Herculis. By comparison, the accretion efficiency of planetesimals in the circumbinary polar protoplanetary disk is lower than that in the coplanar one according to our simulation. So, we can infer the formation of planets in the inner region or around the location where the current debris disk exist is difficult in the system of 99 Herculis.

5. Discussion and Conclusions

5.1. Discussion

The innermost stable orbits simulated by Cuello & Giuppone (2019) and Chen et al. (2020) are located closer to the star (about $2.5a_1$) for their integration times of $10^5 T_1$ and $5 \times 10^4 T_1$, while the integration time is $10^7 T_1$ in our article. Cuello & Giuppone (2019) studied the evolution of misaligned circumbinary disks through hydrodynamical simulations. Viscous torques exerted by the binary make retrograde configurations easier to become polar than prograde circumbinary disks.

Childs & Martin (2021) show that about five circumbinary planets form in polar and coplanar orbits in the vicinity of $5.4a_1$. However, they simulate the late stage of the formation of planets with purely gravitational interactions for Moon-sized planetesimals and Mars-sized embryos. That means every impact can be regarded as a perfectly inelastic collision, which leads to perfect accretion. The physical size of planetesimals in our simulations are distributed in 1–10 km. Various outcomes of collision including perfect accretion, partial accretion, hit-and-runs, graze-and-merges, catastrophic disruptions, and supercatastrophic disruptions have been considered.

A possible third component, which is about 2.4 times as faint as 99 Herculis B, was reported three times (Kennedy et al. 2012). According to the three positions in sky coordinates, the possible stable orbits may be in Kozai cycles. The third component might be involved in the formation of the polar disk of 99 Herculis, which is interesting to study further. Lepp et al. (2023) find out that polar circumtriple orbits only exist within a critical radius, outside which circulating orbits precess about the binary angular momentum vector. Through the smoothed particle hydrodynamics simulations of Ceppi et al. (2023), the wide range of disk inclinations in hierarchical systems with more than two stars may result from the secular oscillation of their orbital parameters. Chen et al. (2022) investigated the orbital dynamics of circumbinary planetary systems with two planets in polar orbits around the binary star. Under binary-planet and planet–planet gravitational interactions, the tilt angles of planets oscillate complicatedly.

The study of planetary formation in this paper is conducted under the framework of the core accretion model. Some giant planets such as the four giants in the HR 8799 system are detected far away from the central star through the method of imaging. If gravity instabilities give rise to collapses in the solid component of the disk material, then giant planets can form in the outer regions of the protoplanetary disk. Planets formed beyond 100 au in solar-like gas disks through disk fragmentation can migrate inward, and produce giant protoplanets at a distance of a few tens of astronomical units from the protostar via high-resolution numerical hydrodynamics simulations (Vorobyov & Elbakyan 2018).

Because typical collisional timescale in the polar disk is at least one order of magnitude longer than the dissipation timescale of the gas disk, it is practically impossible for gas giants to form via the core accretion model. In this model, the formation of planets mainly depends on the collisions among the planetesimals at the early stage. However, we could not exclude the possibilities of other models such as gravitational instability, pebble, or dust accretion producing planets or planet embryos.

5.2. Conclusions

The motion of planetesimals in polar orbits within the libration region of the outer-restricted three-body problem is simulated in this paper to study the stability of circumbinary polar orbits and planetary formation in the circumbinary polar disk of 99 Herculis. First, the empirical formulas of the stable critical semimajor axes of the polar orbits applied to $0.1 \leqslant \lambda \leqslant 1$, $0.0 \leqslant e_1 \leqslant 0.15$, and $0.65 \leqslant e_1 \leqslant 0.8$ in Equation (4), as well as $0.1 \leqslant \lambda \leqslant 1$ and $0.3 \leqslant e_1 \leqslant 0.6$ in Equation (5), are presented. Second, the collision outcomes, colliding timescales, and stochastic simulations of successive collisions among the planetesimals in the polar protoplanetary disk of the 99 Herculis system are statistically analyzed. The statistical results show that the collisions of planetesimals (with physical radii of 1–10 km and density $3\,\mathrm{g\,cm^{-3}}$) in the polar disk are the most unhelpful to the accretion and size increase of planetesimals compared with the coplanar case and the standard case. The typical collisional timescale in the polar disk is at least one order of magnitude higher than the dissipation timescale of the gas disk. Furthermore, collisions of planetesimals in the polar protoplanetary disk of 99 Herculis will not make planetesimals grow, but produce dust steadily, which may explain the formation of the detected debris disk around 120 au. Third, considering the various outcomes of collisions among the planetesimals (1–10 km), the performance of planetesimal growth via collisions in reference groups, including the coplanar case and standard case, are similar. The main differences between the three cases lie in the impact rate and the collision timescales.

ORCID iDs

Ying Wang ⓘ https://orcid.org/0000-0003-0506-054X
Wei Sun ⓘ https://orcid.org/0000-0003-2620-6835
Ji-lin Zhou ⓘ https://orcid.org/0000-0003-1680-2940
Ming Yang ⓘ https://orcid.org/0000-0002-6926-2872

References

Aly, H., Lodato, G., & Cazzoletti, P. 2018, MNRAS, 480, 4738
Artymowicz, P., & Lubow, S. H. 1994, ApJ, 421, 651
Avenhaus, H., Quanz, S. P., Schmid, H. M., et al. 2017, AJ, 154, 33
Batygin, K., & Brown, M. E. 2016, AJ, 151, 22
Brinch, C., Jørgensen, J. K., Hogerheijde, M. R., Nelson, R. P., & Gressel, O. 2016, ApJL, 830, L16
Capelo, H. L., Herbst, W., Leggett, S., Hamilton, C. M., & Johnson, J. A. 2012, ApJL, 757, L18
Cazzoletti, P., Ricci, L., Birnstiel, T., & Lodato, G. 2017, A&A, 599, A102
Ceppi, S., Longarini, C., Lodato, G., Cuello, N., & Lubow, S. H. 2023, MNRAS, 520, 5817
Chen, C., Franchini, A., Lubow, S. H., & Martin, R. G. 2019, MNRAS, 490, 5634
Chen, C., Lubow, S. H., & Martin, R. G. 2020, MNRAS, 494, 4645
Chen, C., Lubow, S. H., & Martin, R. G. 2022, MNRAS, 510, 351
Chiang, E. I., & Murray-Clay, R. A. 2004, ApJ, 607, 913
Childs, A. C., & Martin, R. G. 2021, ApJL, 920, L8

Cuello, N., & Giuppone, C. A. 2019, A&A, 628, A119
Doolin, S., & Blundell, K. M. 2011, MNRAS, 418, 2656
Dvorak, R. 1986, A&A, 167, 379
Farago, F., & Laskar, J. 2010, MNRAS, 401, 1189
Ford, E. B., Kozinsky, B., & Rasio, F. A. 2000, ApJ, 535, 385
Fragner, M. M., & Nelson, R. P. 2010, A&A, 511, A77
Gianuzzi, E., Giuppone, C., & Cuello, N. 2023, A&A, 669, A123
Gong, Y.-X. 2016, ApJ, 834, 55
Haisch, K. E., Jr, Lada, E. A., & Lada, C. J. 2001, ApJL, 553, L153
Harrington, R. S. 1968, AJ, 73, 190
Harrington, R. S. 1969, CeMec, 1, 200
Holman, M. J., & Wiegert, P. A. 1999, AJ, 117, 621
Hong, C., & van Putten, M. H. 2019, arXiv:1905.03605
Hunziker, S., Schmid, H. M., Ma, J., et al. 2021, A&A, 648, A110
Kennedy, G., Wyatt, M., Sibthorpe, B., et al. 2012, MNRAS, 421, 2264
Kennedy, G. M., Matrà, L., Facchini, S., et al. 2019, NatAs, 3, 230
Kenyon, S. J., & Bromley, B. C. 2015, ApJ, 806, 42
Kozai, Y. 1962, AJ, 67, 591
Kral, Q., Matra, L., Wyatt, M. C., & Kennedy, G. M. 2017, MNRAS, 469, 521
Kral, Q., Wyatt, M., Carswell, R., et al. 2016, MNRAS, 461, 845
Lacour, S., Biller, B., Cheetham, A., et al. 2016, A&A, 590, A90
Larwood, J., Nelson, R., Papaloizou, J., & Terquem, C. 1996, MNRAS, 282, 597
Leinhardt, Z. M., & Stewart, S. T. 2011, ApJ, 745, 79
Lepp, S., Martin, R. G., & Lubow, S. H. 2023, ApJ, 943, L4
Li, D., Zhou, J.-L., & Zhang, H. 2014, MNRAS, 437, 3832
Martin, D. V., & Triaud, A. H. 2014, A&A, 570, A91
Martin, R. G., & Lubow, S. H. 2017, ApJL, 835, L28
Martin, R. G., & Lubow, S. H. 2018, MNRAS, 479, 1297
Martin, R. G., & Lubow, S. H. 2019, MNRAS, 490, 1332
Marzari, F., Picogna, G., Desidera, S., & Vanzani, V. 2012, LPI, 1659, 1093
Marzari, F., Thebault, P., Scholl, H., Picogna, G., & Baruteau, C. 2013, A&A, 553, A71
Meschiari, S. 2012, ApJ, 752, 71

Moriwaki, K., & Nakagawa, Y. 2004, ApJ, 609, 1065
Naoz, S., Farr, W. M., Lithwick, Y., Rasio, F. A., & Teyssandier, J. 2013, MNRAS, 431, 2155
Paardekooper, S.-J., Leinhardt, Z. M., Thébault, P., & Baruteau, C. 2012, ApJL, 754, L16
Paardekooper, S.-J., Thebault, P., & Mellema, G. 2008, MNRAS, 386, 973
Pelupessy, F., & Zwart, S. P. 2013, MNRAS, 429, 895
Penzlin, A. B., Kley, W., & Nelson, R. P. 2021, A&A, 645, A68
Pierens, A., & Nelson, R. P. 2013, A&A, 556, A134
Pilat-Lohinger, E., Funk, B., & Dvorak, R. 2003, A&A, 400, 1085
Pilbratt, G., Riedinger, J., Passvogel, T., et al. 2010, A&A, 518, L1
Price, D. J., Cuello, N., Pinte, C., et al. 2018, MNRAS, 477, 1270
Rafikov, R. R. 2013a, ApJL, 764, L16
Rafikov, R. R. 2013b, ApJL, 765, L8
Ribas, Á, Bouy, H., & Merín, B. 2015, A&A, 576, A52
Ribas, Á, Macías, E., Espaillat, C. C., & Duchêne, G. 2018, ApJ, 865, 77
Sano, T., Miyama, S. M., Umebayashi, T., & Nakano, T. 2000, ApJ, 543, 486
Scholl, H., Marzari, F., & Thébault, P. 2007, MNRAS, 380, 1119
Stewart, S. T., & Leinhardt, Z. M. 2012, ApJ, 751, 32
Sutherland, A. P., & Kratter, K. M. 2019, MNRAS, 487, 3288
Thun, D., & Kley, W. 2018, A&A, 616, A47
Umebayashi, T., Katsuma, N., & Nomura, H. 2013, ApJ, 764, 104
Verrier, P., & Evans, N. 2008, MNRAS, 390, 1377
Verrier, P., & Evans, N. 2009, MNRAS, 394, 1721
Vorobyov, E. I., & Elbakyan, V. G. 2018, A&A, 618, A7
Wang, Y., Zhou, J.-l., Liu, F.-y., et al. 2019, MNRAS, 490, 359
Winn, J. N., Holman, M. J., Johnson, J. A., Stanek, K. Z., & Garnavich, P. M. 2004, ApJL, 603, L45
Wyatt, M., & Dent, W. 2002, MNRAS, 334, 589
Wyatt, M. C. 2008, ARA&A, 46, 339
Xie, J.-W., & Zhou, J.-L. 2009, ApJ, 698, 2066
Xie, J.-W., Zhou, J.-L., & Ge, J. 2009, ApJ, 708, 1566
Zanazzi, J., & Lai, D. 2018, MNRAS, 473, 603
Ziglin, S. 1975, SvAL, 1, 194